vehicles

MDPI

Article

Vehicle Trajectory Tracking Control Using MIMO-MPC Combined with IMM-AUKF Road Adhesion Coefficient Estimation

Qiusheng Liu [1,*], Chuanyu Jiang [1], Jian Wang [1,2] and Joan P. Lazaro [3]

[1] School of Automotive Engineering, Jiangxi College of Applied Technology, Ganzhou 341000, China
[2] Faculty of Mechanical Engineering, Universiti Technologi MARA, Shah Alam 40450, Malaysia
[3] Graduate School, University of the East, Manila 1016, Philippines
* Correspondence: liuqiusheng@jxyy.edu.cn

Abstract

This study investigates a simulation-based estimation–control chain that integrates an interactive multiple model adaptive unscented Kalman filter (IMM-AUKF) with a multiple-input multiple-output model predictive controller (MIMO-MPC). A seven-degree-of-freedom vehicle model and a Pacejka tire model are used to represent nonlinear vehicle dynamics. The controller updates model and regression region steering constraints from the estimated adhesion state and jointly allocates front/rear steering and longitudinal force commands. The revised experiments use a 0.5 ms plant integration step and a consistent 20 ms estimator/controller update. Under high-adhesion double lane change (DLC), the proposed chain lowers speed RMSE from 0.7950 to 0.1833 m/s and mean adhesion estimation RMSE from 0.1567 to 0.0812. Under variable-adhesion single lane change (SLC), lateral RMSE decreases from 0.1816 to 0.1649 m, speed RMSE from 0.7983 to 0.2505 m/s, and mean adhesion estimation RMSE from 0.1622 to 0.0949. Heading error is not uniformly improved and is reported as a design trade-off. These results provide reproducible simulation evidence, while hardware-in-the-loop and real-vehicle validation remain future work.

Keywords: MIMO-MPC; IMM-AUKF; adhesion coefficient estimation; vehicle trajectory tracking; dynamic constraints

1. Introduction

Active vehicle safety control must satisfy both trajectory-tracking accuracy and attitude stability under complex driving conditions. In engineering applications, the traditional "lateral model predictive control (MPC) + longitudinal proportional–integral–derivative (PID)" architecture is widely used because of its clear structure and low implementation cost. However, during highly dynamic lane changes and abrupt road adhesion variations, its decoupling assumption cannot fully capture lateral–longitudinal coupling dynamics. For trajectory control problems, Cao et al. [1] improved tracking performance through convex optimization; Cui et al. [2] strengthened stability coordination through steering envelope constraints; Zhang et al. [3] used two-layer learning MPC to improve yaw stability; and Zhang et al. [4] further proposed a constrained adaptive path-following strategy. These studies demonstrate the effectiveness of MPC and constraint design. However, lateral and longitudinal control channels are still commonly designed separately, leaving unified optimization objectives and consistency constraints between longitudinal PID and lateral MPC insufficiently addressed.

Check for updates

Academic Editors: Jiliang Mo and Richard Romano

Received: 19 May 2026
Revised: 28 July 2026
Accepted: 6 August 2026
Published: 2 September 2026

Copyright: © 2026 by the authors. Licensee MDPI, Basel, Switzerland. This article is an open access article distributed under the terms and conditions of the Creative Commons Attribution (CC BY) license.

To mitigate model mismatch, research on road adhesion estimation has continued to develop. Shao et al. [5] verified the feasibility of robust adhesion estimation during steering; Xu et al. [6] performed estimation by fusing dynamics and tire models; Wielitzka et al. [7] added credibility assessment to the unscented Kalman filter (UKF) framework; and Heidfeld et al. [8] constructed a nonlinear UKF observer for 4WD vehicles. On this basis, Fu Xiang et al. [9] introduced a fading memory mechanism to improve estimation performance under time-varying noise. Liu Zhiqiang et al. [10] applied the Sage–Husa approach to adhesion estimation. Luo et al. [11] further improved Sage–Husa-UKF to enhance numerical stability, and Zhang Jiaxu et al. [12] implemented model switching and probability fusion through the interactive multiple model (IMM) mechanism. These studies improve estimation accuracy and operating condition adaptability, but their estimates have not yet been fully converted into online model parameter updates and constraint-boundary information for path-tracking controllers.

Constraint reconstruction under extreme driving conditions is also critical [13–15]. Zheng et al. [16] proposed regression region constraints and showed that recoverable state domain constraints can improve stable recovery during extreme maneuvers, providing a theoretical basis for steering boundary dynamics. Taken together, current studies reveal a key gap—adhesion estimation, lateral–longitudinal coupled control—and online steering constraint updates remain relatively independent, and a unified alternative to the traditional "lateral MPC + longitudinal PID" architecture has not yet been established.

This paper constructs a closed loop linking IMM-AUKF adhesion estimation, regression region steering constraints, and coupled MIMO-MPC allocation. The contribution is the executable information flow: the estimator supplies an online adhesion prior, the constraint layer converts that prior into steering boundaries, and the controller jointly allocates steering and longitudinal force increments. This revised study reports both the benefits and the metric-specific limitations of this integration instead of claiming uniform improvement in all tracking channels.

2. Vehicle System Dynamics Model

2.1. Seven-Degree-of-Freedom Vehicle Model

The seven-degree-of-freedom vehicle dynamics model and the corresponding symbol definitions are shown in Figure 1.

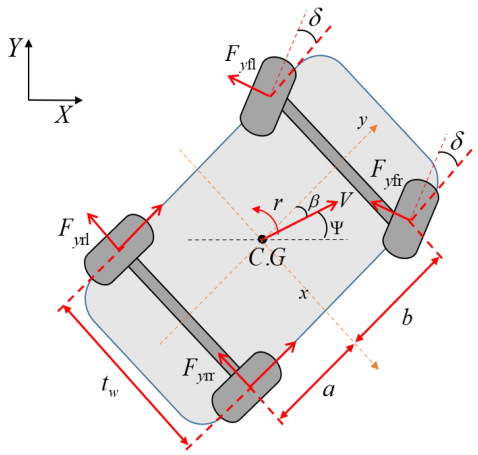


Figure 1. Schematic diagram of the seven-degree-of-freedom vehicle dynamics model.

2.1.1. State Variables, Input Variables, and Modeling Boundaries

This paper adopts a coupled model with three-body plane degrees of freedom and four-wheel rotation degrees of freedom. According to Figure 1, the velocity components

in the vehicle body coordinate system are denoted as $\dot{x}, \dot{y}$, the resultant speed as V, the center-of-mass sideslip angle as β, the yaw angle as Ψ, and the yaw angular velocity as r. The distances from the center of mass to the front and rear axles are denoted as a and b, respectively, and the track width is denoted as t_w.

For readability, the main vehicle state and input symbols are defined when the model is introduced. The global vehicle coordinates are denoted by x_g and y_g; v_x, v_y, and v denote the longitudinal, lateral, and resultant vehicle speeds, respectively; β is the center-of-mass sideslip angle; ψ is the vehicle heading/yaw angle; and r is the yaw angular velocity. The equivalent front and rear axle steering angles are denoted by δ_f and δ_r, the front and rear longitudinal force inputs by F_{xf} and F_{xr}, and the lateral tire force of wheel i by F_{yi}.

$$x = [\dot{x},\ \dot{y},\ r,\ \omega_{fl},\ \omega_{fr},\ \omega_{rl},\ \omega_{rr}]^T \tag{1}$$

$$u = [\delta_f,\ \delta_r,\ F_{x,f},\ F_{x,r}]^T \tag{2}$$

$$V = \sqrt{\dot{x}^2 + \dot{y}^2},\ \beta = \arctan\left(\frac{\dot{y}}{\dot{x}}\right),\ \dot{\Psi} = r \tag{3}$$

$$y = [V,\ Y,\ \Psi]^T \tag{4}$$

where δ_f and δ_r are the equivalent steering angles of the front and rear axles, $F_{x,f}$ and $F_{x,r}$ are the longitudinal force control inputs of the front and rear axles, and $F_{yfl}, F_{yfr}, F_{yrl}, F_{yrr}$ denotes the four-wheel lateral forces.

2.1.2. Body Dynamics and Wheel Speed Equations

In the vehicle body coordinate system, translational and rotational dynamics satisfy the Newton–Euler equations. According to the force and geometric relationships shown in Figure 1, the governing equations are obtained as follows:

$$m(\ddot{x} - \dot{y}r) = F_{xfl} + F_{xfr} + F_{xrl} + F_{xrr} \tag{5}$$

$$m(\ddot{y} + \dot{x}r) = F_{yfl} + F_{yfr} + F_{yrl} + F_{yrr} \tag{6}$$

$$I_z\dot{r} = a(F_{yfl} + F_{yfr}) - b(F_{yrl} + F_{yrr}) + \frac{t_w}{2}(F_{xfr} - F_{xfl} + F_{xrr} - F_{xrl}) \tag{7}$$

$$J_w\dot{\omega}_i = T_i - R_wF_{x,i},\ i \in \{fl, fr, rl, rr\} \tag{8}$$

where T_i is the wheel-end driving/braking torque, and R_w is the effective wheel radius. The above equations provide a unified coupling relationship among vehicle lateral–longitudinal motion, yaw motion, and four-wheel rotation.

In the wheel dynamics notation, T_w denotes the wheel-end driving/braking torque, and R_w denotes the effective wheel radius.

2.1.3. Kinematic Equations and Discretization

To evaluate trajectory tracking, the vehicle body velocity must be mapped to the global coordinate system (X, Y). Using the heading angle Ψ in Figure 1, the kinematic equations are given as follows:

$$\dot{X} = \dot{x}\cos\Psi - \dot{y}\sin\Psi\ \dot{Y} = \dot{x}\sin\Psi + \dot{y}\cos\Psi,\ \dot{\Psi} = r \tag{9}$$

$$x_{k+1} = f(x_k, u_k) \tag{10}$$

In the following controller derivation, to remain consistent with the notation of the discrete prediction model, $\dot{x}, \dot{y}, \Psi$ is often denoted as V_x, V_y, ϕ, respectively. This is only a notation mapping and does not change the physical meaning.

2.2. Pacejka Tire Model

2.2.1. Pure Longitudinal Tire Force Model

The longitudinal tire force is described by the Pacejka Magic Formula, which provides a continuous and differentiable representation over both small- and large-slip ranges. This model is essential for longitudinal acceleration, deceleration, and speed error control.

$$q_x = B_x\kappa - E_x(B_x\kappa - \arctan(B_x\kappa))\ F_{x0} = D_x \sin(C_x \arctan(q_x)) \tag{11}$$

$$D_x = \mu_x F_z,\ B_x = \frac{K_{x\kappa}}{C_x D_x} \tag{12}$$

Parameters B_x, C_x, D_x, E_x correspond to stiffness, shape, peak value and curvature respectively, and can be obtained by fitting test data.

2.2.2. Pure Lateral Tire Force Model

The lateral tire force model characterizes the coupling between steering input and yaw response. By taking the slip angle as the input, the model describes nonlinear tire behavior from the linear region to the saturation region.

$$q_y = B_y\alpha - E_y(B_y\alpha - \arctan(B_y\alpha))\ F_{y0} = D_y \sin\big(C_y \arctan(q_y)\big) \tag{13}$$

$$D_y = \mu_y F_z,\ B_y = \frac{K_{y\alpha}}{C_y D_y} \tag{14}$$

In MIMO-MPC, the lateral tire model affects not only prediction accuracy but also the calculation of dynamic constraint boundaries.

2.2.3. Combined Slip and Coordinate Transformation

Under real driving conditions, tires often operate in a combined longitudinal–lateral slip state. This paper uses a combined slip correction coefficient and transforms tire coordinate forces into the vehicle body coordinate system to ensure closed-loop consistency of the dynamic equations.

$$F_x = \mu G_{x\alpha} F_{x0},\ F_y = \mu G_{y\kappa} F_{y0} \tag{15}$$

$$F_{x,i} = F_{t,i}\cos\delta_i - F_{s,i}\sin\delta_i \tag{16}$$

$$F_{y,i} = F_{t,i}\sin\delta_i + F_{s,i}\cos\delta_i \tag{17}$$

This transformation is consistent with the adhesion estimation observation model and provides an important basis for the coordinated design of the estimator and controller.

3. IMM-AUKF Road Adhesion Coefficient Estimation Algorithm

3.1. Road Adhesion Coefficient Estimation Based on UKF

3.1.1. State Space Modeling and Observation Structure

The road adhesion coefficient cannot be measured directly. This paper treats the four-wheel adhesion coefficients as estimated states and uses a random walk process to describe their time-varying characteristics. This formulation ensures state identifiability and supports consistent coupling with the nonlinear tire model and the vehicle dynamics equations [5,7,17].

$$x_k = [\mu_{fl},\ \mu_{fr},\ \mu_{rl},\ \mu_{rr}]_k^T \tag{18}$$

$$x_{k+1} = x_k + w_k,\ w_k \sim \mathcal{N}(0, Q_k) \tag{19}$$

$$z_k = h(x_k, \chi_k) + v_k,\ v_k \sim \mathcal{N}(r_k, R_k) \tag{20}$$

$$\mu_i \in [\mu_{min}, \mu_{max}],\ i \in \{fl, fr, rl, rr\} \tag{21}$$

where x_k consists of the four-wheel adhesion coefficients and reflects the current tire–road interaction capability of the vehicle. The state equation adopts a random walk model based on the assumption that the adhesion coefficient changes slowly and is affected by unmodeled disturbances; therefore, the process noise w_k is used to characterize uncertain road surface disturbances.

The scalar μ_i denotes the road adhesion coefficient of wheel i, and the four-wheel adhesion vector is used as the estimated state in the observer.

The observation equation is constructed from the relationship between the seven-degree-of-freedom dynamics and tire forces. $h(\cdot)$ maps the adhesion state to measurable quantities, such as acceleration and wheel speed change rate; v_k is the measurement noise. Interval constraints ensure that the estimates remain within the physically feasible range and prevent the filter from entering a meaningless solution domain under noise excitation.

Here, χ_k represents the set of exogenous variables composed of vehicle speed, yaw angular velocity, wheel speed, drive/braking input, and steering angle. By explicitly imposing adhesion state boundaries in the filtering process, the estimates are prevented from entering physically meaningless regions.

3.1.2. Unscented Transformation and Prediction Update

The UKF propagates Sigma points to approximate the evolution of nonlinear probability distributions and avoid Jacobian linearization errors. This paper uses standard unscented transformation (UT) parameterization and preserves second-order statistics to improve filtering stability during abrupt adhesion changes.

$$\lambda = \alpha^2(n + \kappa) - n \tag{22}$$

Equation (22) defines the unscented transformation scaling parameter λ, which controls the spread of the Sigma points relative to the prior covariance.

$$W_0^m = \frac{\lambda}{n + \lambda},\ W_0^c = \frac{\lambda}{n + \lambda} + 1 - \alpha^2 + \beta \tag{23}$$

Equation (23) gives the weight of the central Sigma point in mean and covariance propagation, where β injects prior information about the distribution shape.

$$W_i^m = W_i^c = \frac{1}{2(n + \lambda)},\ i = 1, \ldots, 2n \tag{24}$$

Equation (24) defines the weights of the non-central Sigma points, ensuring that all sampling point weights are normalized and satisfy second-order statistical consistency.

$$\chi_k^{(0)} = \hat{x}_k,\ \chi_k^{(i)} = \hat{x}_k \pm \left(\sqrt{(n + \lambda)P_k}\right)_i \tag{25}$$

Equation (25) gives the Sigma point construction rule. With the prior mean as the center, the sampling points are symmetrically expanded along the principal directions of the covariance.

$$\hat{x}_{k+1|k} = \sum_{i=0}^{2n} W_i^m f(\chi_k^{(i)}, u_k) \tag{26}$$

Equation (26) describes state prediction: each Sigma point is propagated through the system function and then weighted to obtain the prior state mean.

$$\hat{z}_{k+1|k} = \sum_{i=0}^{2n} W_i^m h(\chi_{k+1|k}^{(i)}, u_k) \tag{27}$$

Equation (27) describes observation prediction: the predicted Sigma points are mapped into the observation space and then weighted to obtain the prior observation mean.

$$P_{zz,k+1} = \sum_{i=0}^{2n} W_i^c \Delta z_i \Delta z_i^T + R_k \tag{28}$$

Equation (28) calculates the predicted observation covariance $P_{zz,k+1}$, which is obtained by superposing the Sigma point variance and the measurement noise covariance.

$$K_{k+1} = P_{xz,k+1} P_{zz,k+1}^{-1} \tag{29}$$

Equation (29) gives the Kalman gain, which determines the fusion weight between model prediction and actual observation during state update.

$$\hat{x}_{k+1|k+1} = \hat{x}_{k+1|k} + K_{k+1}(z_{k+1} - \hat{z}_{k+1|k}) \tag{30}$$

Equation (30) gives the posterior state update formula, in which the innovation term corrects the prior estimate to obtain the current posterior adhesion coefficient.

The above derivation is based on the unscented transform. $\lambda, \alpha, \beta, \kappa$ determines the Sigma point distribution and weighting scheme, with the goal of preserving the mean and covariance propagation accuracy of the nonlinear system without explicitly computing the Jacobian.

Sigma points are generated from the prior mean and the square root matrix of the covariance, thereby forming a deterministic set of samples in the state space. After propagation through the nonlinear functions $f(\cdot)$ and $h(\cdot)$, the predicted state and predicted observation are obtained.

$P_{zz,k+1}$ is the predicted observation covariance, K_{k+1} is the Kalman gain, and the final step is a standard Bayesian correction in which the prior state is corrected by the observation residual $z_{k+1} - \hat{z}_{k+1|k}$ to obtain the posterior estimate.

This paper sets $\alpha = 10^{-3}, \beta = 2, \kappa = 0$ and combines covariance symmetrization with minimum eigenvalue truncation to reduce the risk of numerical divergence caused by ill-conditioned matrices.

3.2. AUKF Algorithm Based on Sage–Husa Noise Estimation

3.2.1. Time-Varying Noise Modeling

Vehicle sensing noise varies significantly during braking, steering, and adhesion switching. Fixed noise assumptions reduce the weight assigned to new observations and may delay convergence. This paper introduces an improved Sage–Husa adaptive UKF (AUKF) estimator that updates only the measurement noise statistics online, thereby enhancing the filter response to sudden changes in driving conditions [11,17].

$$d_{k+1} = \frac{1-b}{1-b^{k+1}},\ 0.95 < b < 0.99 \tag{31}$$

$$r_{k+1} = (1 - d_{k+1}) r_k + d_{k+1}(z_{k+1} - \hat{z}_{k+1|k}) \tag{32}$$

$$\tilde{y}_{k+1|k} = z_{k+1} - \hat{z}_{k+1|k} \tag{33}$$

$$E_{R,k+1} = \tilde{y}_{k+1|k}\tilde{y}_{k+1|k}^{T} - P_{zz,k+1|k}R_{k+1} = (1 - d_{k+1})R_k + d_{k+1}E_{R,k+1} \tag{34}$$

This set of formulas follows the Sage–Husa adaptive noise estimation principle. d_{k+1} is a time-varying weight: it is larger at the beginning of the iteration to emphasize new observations and gradually decreases later to suppress noise fluctuation.

r_{k+1} corresponds to the observation noise mean update, and $\tilde{y}_{k+1|k}$ is the innovation vector. $E_{R,k+1}$ is obtained by subtracting the predicted observation covariance from the innovation outer product, which reflects the mismatch between the current observed noise intensity and the model prediction; updating R_{k+1} accordingly enables the filter noise statistics to adapt online to changing driving conditions.

Here, b is the forgetting factor. A larger b increases the weight of new data. This paper sets $b = 0.98$ to balance rapid tracking during abrupt changes with variance suppression during steady-state intervals.

In the implemented setting, b = 0.98 is used for the Sage–Husa adaptive update. This value gives a high memory weight to historical noise statistics while still allowing new innovation information to correct the measurement noise estimate. If b is too small, the covariance update becomes sensitive to transient outliers and may cause noise oscillation; if b is too close to 1, the estimator responds slowly to abrupt adhesion changes. Therefore, b = 0.98 is selected as a compromise between adaptation speed and covariance smoothness.

3.2.2. Numerical Stability and Positive Definite Correction

To avoid filter divergence caused by the loss of positive definiteness in the noise covariance of high-order systems, this paper performs symmetrization and diagonal projection correction after each noise update. This treatment preserves the physical interpretability of R_k and enhances numerical robustness under low-adhesion and split road conditions.

$$R_{k+1} = (1 - \lambda_k)R_k + \lambda_k(e_{k+1}e_{k+1}^{\mathrm{T}} - R_{k+1}) \tag{35}$$

$$R_{k+1}^{(1)} = 1/2(R_{k+1} + R_{k+1}^{\mathrm{T}}) = V\Lambda\, V^{\mathrm{T}} \tag{36}$$

$$R_{k+1} = V\ diag(max(\lambda_{\mathrm{i}}, \varepsilon))V^{\mathrm{T}} \tag{37}$$

The correction is applied in a causal order. First, the raw covariance update is formed from the previous covariance and the current innovation. Second, the raw matrix is symmetrized. Third, its eigenvalues are floored at ε and the matrix is reconstructed. Thus, the update contains no algebraic self-reference, and the resulting covariance is symmetric positive semidefinite.

The above correction ensures that the measurement noise matrix satisfies the positive semi-definite condition, thereby allowing the Kalman gain calculation and state update process to remain stable.

3.3. Adaptive Operating Condition Estimation Based on an Interactive Multiple Model

3.3.1. Dual-Model IMM Structure

Considering differences in observable excitation across driving conditions, this paper constructs a dual-model IMM structure. Model 0 is used for longitudinally dominant conditions, whereas Model 1 is used for lateral–longitudinal coupled conditions. Through condition dependent observation vectors, observability is maintained under weak excitation and estimation accuracy is improved under strong coupling [12,17].

$$z_x = [a_x,\ \dot{\omega}_1,\ \dot{\omega}_2,\ \dot{\omega}_3,\ \dot{\omega}_4]^T \tag{38}$$

$$z_{xy} = [a_x,\ a_y,\ \gamma,\ 0,\ 0]^T \tag{39}$$

$$\Delta\mu_l = \mu_{fl}^{est} - \mu_{rl}^{est},\ \Delta\mu_r = \mu_{fr}^{est} - \mu_{rr}^{est} \tag{40}$$

$$z_{xy,4} = \Delta\mu_l \approx 0,\ z_{xy,5} = \Delta\mu_r \approx 0 \tag{41}$$

$$\Pi = [p_{ij}]_{2\times 2},\ \sum_j p_{ij} = 1 \tag{42}$$

$$p_{00} = p_{11} = 0.8,\ p_{01} = p_{10} = 0.2 \tag{43}$$

where z_x is designed for longitudinally excited scenarios and mainly uses longitudinal acceleration and wheel speed dynamics to establish observations; z_{xy} is designed for lateral–longitudinal coupled scenarios and adds lateral acceleration and yaw response to improve observability.

$\Delta\mu_l, \Delta\mu_r$ is used to construct the coaxial left and right wheel adhesion consistency constraints, reflecting the prior that "the wheel adhesion on the same side is approximately consistent in a short time", where the superscript ^{est} represents the estimated value. The transfer matrix Π is derived from Markov chain modeling. Its larger diagonal elements indicate stronger working condition persistence, and non-diagonal elements are used to retain the ability to switch working conditions.

This transition probability matrix reflects the balance between stable condition memory and switching flexibility. It maintains model memory in stable intervals while retaining switching flexibility during abrupt changes.

The dual-model configuration is not intended to assign one sub-model to every possible road surface. Instead, it separates the two dominant observation mechanisms that affect adhesion observability: longitudinal excitation and lateral–longitudinal coupled excitation. Different road adhesion levels are represented by continuous likelihood changes and posterior probability redistribution inside these two excitation modes. Increasing the number of sub-models can describe more nominal surfaces, but it also increases computation and may cause probability fragmentation when the excitation difference among adjacent models is weak. Therefore, the two-model structure is adopted as a balance between adaptability, numerical stability, and real-time implementation, while the framework can be extended by adding specialized sub-models for split-adhesion or extremely low-friction surfaces.

3.3.2. Model Interaction and Probability Update

The prior mixing probability is calculated as follows:

$$\bar{c}_j(k-1) = \sum_{i=1}^{r} p_{ij}\mu_i(k-1) \tag{44}$$

Equation (44) calculates the prior mixing probability $\bar{c}_j$ of Model j, which reflects the prediction weight after the transition probability and the previous model probability are jointly applied.

$$\mu_{i|j}(k-1) = \frac{p_{ij}\mu_i(k-1)}{\bar{c}_j(k-1)} \tag{45}$$

Equation (45) gives the conditional probability weight mixed from Model i to Model j, which is used to construct the initial interaction value of Model j.

$$\hat{x}_{0j}(k-1) = \sum_{i=1}^{r} \mu_{i|j}(k-1)\hat{x}_i(k-1) \tag{46}$$

Equation (46) linearly combines the state estimates of all models according to the conditional weights to obtain the interactive initial state of Model j.

$$\Delta P_{ij} = P_i + \Delta x_{ij} \Delta x_{ij}^T \; P_{0j}(k-1) = \sum_{i=1}^{r} \mu_{i|j}(k-1) \Delta P_{ij} \tag{47}$$

Equation (47) gives the interactive initial covariance of Model j, where ΔP_{ij} contains both intra-model covariance and the dispersion term caused by mean shifts.

$$e_{j,k} = -\frac{1}{2} \nu_{j,k}^T S_{j,k}^{-1} \nu_{j,k} \tag{48}$$

Equation (48) defines the Gaussian likelihood exponent, where $\nu_{j,k}$ is the innovation vector and $S_{j,k}$ is the innovation covariance.

$$\Lambda_{j,k} = \frac{1}{(2\pi)^{n/2} \left| S_{j,k} \right|^{1/2}} \exp(e_{j,k}) \tag{49}$$

Equation (49) calculates the observation likelihood of Model j to measure how well the model explains the current observation data.

$$\mu_{j,k} = \frac{\Lambda_{j,k} \bar{c}_j}{\sum_{l=1}^{r} \Lambda_{l,k} \bar{c}_l} \tag{50}$$

Equation (50) gives the posterior model probability update, which combines the prior probability and observation likelihood according to Bayes' rule.

$$\hat{x}_k = \sum_{j=1}^{r} \mu_{j,k} \hat{x}_{j,k} \tag{51}$$

Equation (51) weights the posterior states of all sub-models by their posterior probabilities to obtain the global state estimate after IMM fusion.

$$P_k = \sum_{j=1}^{r} \mu_{j,k} \left(P_{j,k} + \Delta \hat{x}_{j,k} \Delta \hat{x}_{j,k}^T \right) \tag{52}$$

Equation (52) jointly weights the covariance and the mean dispersion terms of each sub-model to obtain the global uncertainty description after IMM fusion.

The above interaction formulas follow a Bayesian probability update procedure. $\bar{c}_j$ is the prior probability of Model j, $\mu_{i|j}$ is the conditional mixing weight from Model i to Model j, and $\hat{x}_{0j}$, P_{0j} corresponds to the mixed initial state and covariance.

$\Lambda_{j,k}$ is obtained from the Gaussian likelihood function and measures the ability of Model j to explain the current observation. The posterior model probability $\mu_{j,k}$ is obtained by normalizing the prior probability multiplied by the likelihood. The final state and covariance fusion adopts the total probability and total covariance formulas to ensure that the fused result is unbiased in a probabilistic sense.

This process forms a closed-loop estimation chain of "interactive initialization, parallel AUKF update, and probabilistic fusion output", enabling the estimator to transfer weights quickly and maintain output continuity when model mismatch occurs.

Equations (44)–(52) can therefore be interpreted as a complete derivation from Markov prediction to Bayesian correction. The previous model probability is first propagated by the transition matrix to obtain the prior probability. Conditional mixing probabilities then

generate the interactive initial state and covariance for each AUKF branch. After the branch filters produce innovations and innovation covariance matrices, the Gaussian likelihood evaluates the consistency between each model and the current observation. The posterior model probabilities are finally obtained by normalizing the product of prior probabilities and likelihoods, and the global adhesion estimate is calculated by probability-weighted state and covariance fusion.

Figure 2 shows the data interaction relationship between the IMM-AUKF adhesion-estimation module and the vehicle model. The "body and tire model, customized road model, and seven-degree-of-freedom model" on the left provide the key inputs required for estimation, including steering angle, vehicle speed state, wheel speed, longitudinal and lateral acceleration, and wheel-end torque.

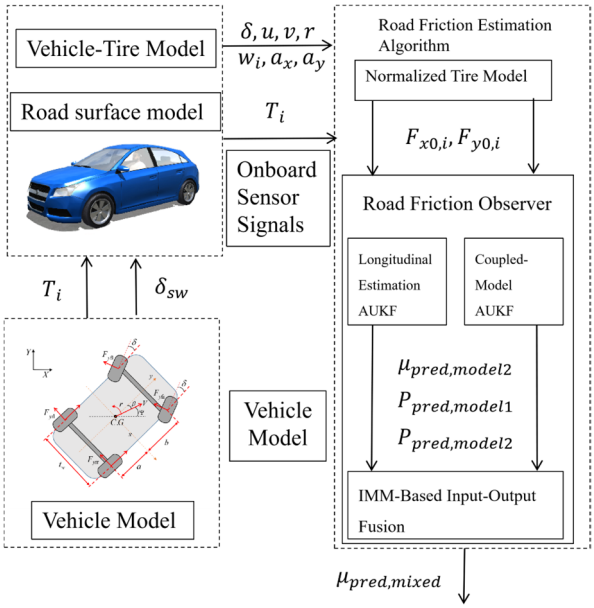


Figure 2. Schematic diagram of the IMM-AUKF algorithm.

In the estimation link on the right, the $F_{x0,i}$, $F_{y0,i}$ required by the observation structure is first obtained through the tire normalization model. The road adhesion coefficient observer then runs the longitudinal model AUKF and the coupled model AUKF in parallel, outputting $\mu_{pred,model1}$, $\mu_{pred,model2}$ and the corresponding covariance $P_{pred,model1}$, $P_{pred,model2}$, respectively.

Finally, the interactive multiple model (IMM) module completes probability fusion and outputs $\mu_{pred,mixed}$ as the road adhesion estimate. Because Figure 2 details the internal estimator process, the following control chapters use this part as the adhesion estimation input module.

4. MIMO-MPC Trajectory Tracking Controller Design

The overall architecture of the path tracking control algorithm is shown in Figure 3. The figure abstracts the estimation module at the system level and highlights the interfaces among IMM-AUKF, MIMO-MPC, and the execution layer.

In this architecture, vehicle sensing and tire force information enter the IMM-AUKF module to generate adhesion estimates. These estimates update the MIMO-MPC model parameters and regression region constraint boundaries online. After the controller outputs the front and rear axle steering angles and longitudinal driving forces, the actuator-coordination layer performs steering, braking, and driving execution, forming an estimation–decision–execution closed loop.

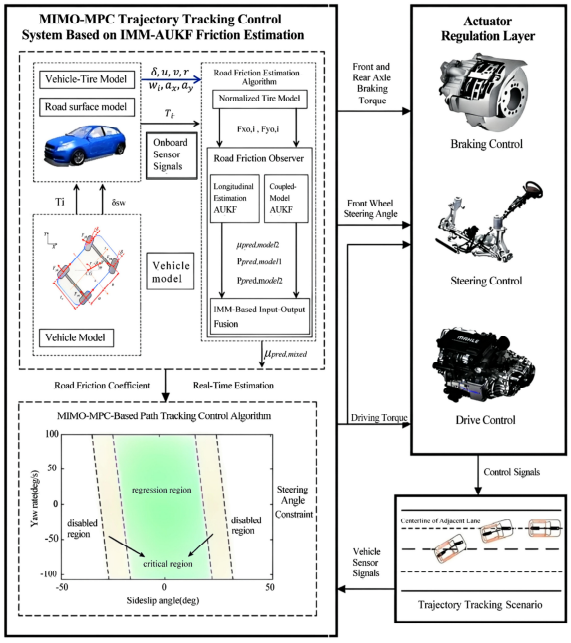


Figure 3. Schematic diagram of the overall control algorithm architecture.

4.1. Prediction Model and Cost Function

4.1.1. Extended State and Linear Time-Varying Prediction Model

To address the inconsistent objectives and unsynchronized constraints of the traditional "lateral MPC + longitudinal PID" architecture under highly dynamic conditions, this paper constructs a lateral–longitudinal integrated MIMO-MPC controller. The controller solves the front and rear axle steering angles and longitudinal forces within the same optimization problem, so that trajectory error, heading error, and speed error are coordinated and converged through a unified cost function [18–20].

$$x = [V_x,\ V_y,\ r,\ X,\ Y,\ \phi]^T \tag{53}$$

$$u = [\delta_f,\ \delta_r,\ F_{x,f},\ F_{x,r}]^T \tag{54}$$

$$y = [V_x,\ Y,\ \phi]^T \tag{55}$$

$$\xi_k = [x_k^T,\ u_{k-1}^T]^T \tag{56}$$

$$\xi_{k+1} = A_{\xi,k}\xi_k + B_{\xi,k}\Delta u_k + d_{\xi,k} \tag{57}$$

$$y_{k+i|k} = C_{\xi,k+i}\xi_{k+i|k} \tag{58}$$

The above model is obtained by first-order linearization and discretization of nonlinear vehicle dynamics at the operating point. After incorporating u_{k-1} into the extended state ξ_k, the optimization variable is converted from "absolute control amount" to "control increment Δu_k", which facilitates the direct application of actuator change rate constraints.

Here, $A_{\xi,k}, B_{\xi,k}$ is a time-varying matrix that changes with the driving condition, $d_{\xi,k}$ absorbs linearization truncation errors and constant terms, and $C_{\xi,k+i}$ maps the extended state to the speed–trajectory–heading output space.

The adopted prediction model is a linear time-varying (LTV) model rather than a fixed linear time-invariant approximation. At each sampling instant, the nonlinear vehicle model is relinearized around the current estimated state and the previous control input, and the resulting matrices are updated before the quadratic program is solved. The affine term in

the prediction model absorbs the constant component and the first-order truncation residue around the operating point.

The influence of linearization error is limited by three mechanisms. First, the prediction horizon is short and the optimization is updated in a receding horizon manner, so prediction mismatch is corrected in the next control cycle. Second, the adhesion-dependent cornering stiffness parameters are updated online by IMM-AUKF, reducing the dominant model parameter error during adhesion changes. Third, absolute and incremental input constraints suppress aggressive control changes when the local linear model becomes less accurate. Therefore, the linearization error mainly appears as a transient heading channel trade-off under abrupt adhesion switching, rather than as a persistent trajectory tracking divergence.

Here, $N_x = 6$, $N_u = 4$, and $N_y = 3$ are defined in the extended-state model. By incorporating the previous control variable into the extended state, the incremental decision variable directly corresponds to the actuator change rate constraint, thereby ensuring implementability and numerical stability.

4.1.2. Model Update Driven by IMM-AUKF Adhesion Estimation

In the prediction layer, the Pacejka Magic Formula branch is used to construct the adhesion-dependent prediction model. IMM-AUKF outputs four-wheel adhesion estimates in each control cycle and forms equivalent adhesion inputs as follows:

$$\overline{\mu}_k = \frac{1}{4} \sum_{i \in \{fl,fr,rl,rr\}} \hat{\mu}_{i,k} \tag{59}$$

At the prediction model layer, the equivalent cornering stiffnesses of the front and rear axles are calculated online using the Pacejka cornering stiffness parameterization (Kya):

$$\eta(F_z) = \frac{F_z / F_{z0}}{PKY_2 + PKY_5 \sin^2 \gamma} \tag{60}$$

$$s_\gamma = 1 - PKY_3 |\sin \gamma| G_\alpha(F_z) = PKY_1 F_{z0} s_\gamma \sin(PKY_4 \arctan \eta(F_z)) \tag{61}$$

$$\tilde{C}_{\alpha f} = |G_\alpha(F_{z,f})|,\ \tilde{C}_{\alpha r} = |G_\alpha(F_{z,r})| \tag{62}$$

$$A_{\xi,k} = A_\xi \left(\tilde{C}_{\alpha f}, \tilde{C}_{\alpha r}, V_x, V_y, r, \delta_f, \delta_r \right) \tag{63}$$

$$B_{\xi,k} = B_\xi \left(\tilde{C}_{\alpha f}, \tilde{C}_{\alpha r}, F_{x,f}, F_{x,r} \right) \tag{64}$$

This set of formulas is derived from Pacejka cornering stiffness parameterization. $\eta(F_z)$ describes the normalized normal load term, s_γ describes the camber correction term, and $G_\alpha(F_z)$ gives the equivalent cornering stiffness function under the current load.

The $A_{\xi,k}, B_{\xi,k}$ update driven by $\tilde{C}_{\alpha f}, \tilde{C}_{\alpha r}$ embodies "estimate model linkage": when changes in adhesion cause changes in available cornering stiffness, the prediction model changes simultaneously, thereby reducing prediction bias caused by model mismatch.

At the constraint layer, the adhesion estimates from IMM-AUKF are converted into steering boundary reconstruction through the regression region thresholds: $\alpha_{f,p}(k) = \arctan\left(\frac{3\overline{\mu}_k F_{z,f}}{C_f}\right)$, $\alpha_{r,p}(k) = \arctan\left(\frac{3\overline{\mu}_k F_{z,r}}{C_r}\right)$. Therefore, this paper forms a dual-channel coupling mechanism of "Pacejka model parameter update + IMM adhesion-constraint update".

4.1.3. Prediction Horizon, Reference Look-Ahead, and Cost Function

To balance real-time calculation and prediction accuracy, the revised controller uses a short receding horizon with Np = 8 and Nc = 1. Reference trajectories are generated in a look-ahead manner:

The revised controller uses a 20 ms estimator/controller period, Np = 8 and Nc = 1. Np = 8 provides 0.16 s of preview while retaining a compact online QP. The one-step control horizon preserves receding horizon feedback and keeps the decision vector small. The regression region slack variable is limited to 2 deg and is available only for the steering regression bounds; physical steering and longitudinal force bounds remain hard constraints.

In the revised simulations, Np = 8 and Nc = 1 are used consistently. The 0.16 s prediction window is retained after checking tracking behavior and online calculation time, while the single-step control horizon keeps the decision vector compact and is updated by receding horizon feedback at every 20 ms sample.

The slack variable penalty is ρ = 1000. It is paired with a 2 deg upper bound and is applied only to the regression region steering rows. This design permits a small, explicitly bounded relaxation when the estimated adhesion causes an abrupt boundary shrinkage, while preventing the slack variable from overriding physical actuator limits.

Controller tuning was conducted sequentially. The 20 ms update, physical actuator limits, increment limits, and adhesion-dependent steering bounds were fixed first. Candidate horizons were then checked for tracking and calculation time; Np = 8 and Nc = 1 were retained. Output error and increment weights were adjusted to avoid persistent oscillation, and ρ = 1000 with a 2 deg slack cap was selected so that regression-bound relaxation remains limited. The same final parameter set was used in both scenarios.

$$\dot{X} = V_x \cos\phi - V_y \sin\phi \; X_{k+p|k} = X_k + pT\dot{X}_k, \; p = 1, \ldots, N_p \tag{65}$$

Equation (65) gives the update rule of the longitudinal coordinates of the look-ahead point: the future p step position is calculated from the current longitudinal velocity projection.

$$[V_{x,k+p}^{ref}, Y_{k+p}^{ref}, \phi_{k+p}^{ref}]^T = \mathcal{R}(X_{k+p|k}) \tag{66}$$

Equation (66) represents the reference mapping function $\mathcal{R}(\cdot)$, which extracts the corresponding speed, lateral position, and heading angle reference values from the look-ahead coordinates.

$$\mathbf{Y}_k = \mathbf{\Phi}_k \xi_k + \mathbf{\Gamma}_k \Delta \mathbf{U}_k + \mathbf{\Psi}_k \tag{67}$$

Equation (67) gives the stacked prediction output equation, in which the multi-step output over the prediction horizon is written as a linear mapping of the current extended state and the control increment sequence.

$$J_y = \sum_{i=1}^{N_p} \| y_{k+i|k} - y_{k+i}^{ref} \|_Q^2 \tag{68}$$

Equation (68) defines the tracking error cost term J_y, which penalizes deviations between the predicted output and the reference trajectory over the entire prediction horizon.

$$J_u = \sum_{i=0}^{N_c-1} \| \Delta u_{k+i|k} \|_{R_{base}}^2 \tag{69}$$

Equation (69) defines the control incremental cost term J_u, which is used to limit the actuator action range and improve control smoothness.

$$J = J_y + J_u + w_c (F_{x,f} - F_{x,r})^2 + \rho \varepsilon^2 \tag{70}$$

Equation (70) gives the overall objective function. In addition to tracking and smoothing terms, it includes a front-rear axle longitudinal force consistency penalty and a slack variable penalty.

$$Q = \mathrm{diag}\left(\frac{1}{0.5^2}, \frac{1}{0.025^2}, \frac{1}{(0.5\pi/180)^2}\right) \tag{71}$$

Equation (71) gives the output error weight matrix, corresponding to the weights of speed, lateral displacement, and heading angle errors.

In the cost function notation, Q denotes the output error weight matrix used for speed, lateral position, and heading angle tracking, whereas R denotes the control increment weight matrix used to penalize steering and longitudinal force variations.

$$r_{\delta f} = \frac{0.5}{\delta_{f,lim}^2},\ r_{\delta r} = \frac{1}{\delta_{r,lim}^2} \tag{72}$$

Equation (72) defines the front and rear axle steering increment penalty coefficients, which are normalized by the upper limits of the corresponding available steering angles.

$$r_{Ff} = \frac{1}{(T_{f,max}/R_w)^2},\ r_{Fr} = \frac{1}{(T_{r,max}/R_w)^2} \tag{73}$$

Equation (73) defines the longitudinal force increment penalty coefficients of the front and rear axles, which are normalized by the maximum available driving/braking capacity.

$$R_{base} = \mathrm{diag}(r_{\delta f}, r_{\delta r}, r_{Ff}, r_{Fr}) \tag{74}$$

Equation (74) constructs the basic control weight matrix R_{base} to organize the incremental costs of the four control channels in a unified form.

$$R = R_{base} + R_{consistency} \tag{75}$$

Equation (75) gives the final input weight matrix, representing the superposition of the basic weight and the consistency coupling weight.

$$\Delta u_k^T R_{consistency} \Delta u_k = w_c(\Delta F_{x,f} - \Delta F_{x,r})^2 \tag{76}$$

Equation (76) is the equivalent quadratic expression of the consistency term, which suppresses conflict between the longitudinal force distributions of the front and rear axles.

$$J_{quad} = \frac{1}{2}\Delta \mathbf{U}_k^T H \Delta \mathbf{U}_k + f^T \Delta \mathbf{U}_k \tag{77}$$

Equation (77) organizes the objective function into a standard quadratic form, where H is the Hessian matrix and f is the linear term coefficient.

$$J_{qp} = J_{quad} + \frac{1}{2}\rho\varepsilon^2 \tag{78}$$

Equation (78) adds a slack variable penalty to the quadratic objective, forming a soft-constrained optimization objective function.

$$\min_{\Delta \mathbf{U}_k, \varepsilon} J_{qp} \tag{79}$$

Equation (79) gives the decision objective of the optimization problem, namely the joint solution of the control increment sequence and slack variables.

$$A_{\Delta u}\Delta \mathbf{U}_k \leq b_{\Delta u},\ \varepsilon \geq 0 \tag{80}$$

Equation (80) gives the incremental constraints and the non-negativity constraint of the slack variable, limiting the control change rate and preserving the physical meaning of the slack variable.

$$A_u\Delta \mathbf{U}_k \leq b_u + \mathbf{1}\varepsilon \tag{81}$$

Equation (81) defines the bounded soft regression region steering constraint. The slack variable ε is non-negative, limited to 2 deg, and does not relax the physical steering or longitudinal force limits.

The first two equations give the reference look-ahead and predicted output stacking relationships, respectively; J_y and J_u describe the tracking error cost and control increment cost, respectively; and $w_c(F_{x,f} - F_{x,r})^2$ suppresses conflict between the longitudinal forces of the front and rear axles.

Q, R_{base} is derived from a weighted quadratic design and reflects the trade-off between error penalization and control smoothing. By introducing the slack variable ε, hard-constrained optimization is converted into soft-constrained optimization, which keeps the problem feasible under extreme conditions.

J_{quad} is the standard quadratic objective, and $A_{\Delta u}, A_u$ corresponds to the incremental and absolute boundaries, respectively. This modeling allows the problem to be directly mapped to convex quadratic programming and solved online.

This paper sets the slack weight to $\rho = 1000$. The objective function uses the consistency penalty term to suppress conflict between the longitudinal forces of the front and rear axles and to avoid local oscillations caused by mutual restraint between lateral and longitudinal control.

4.1.4. Quadratic Programming Standard Form and Online Solution

After the absolute control input constraints are converted into constraints on incremental optimization variables, the control problem can be transformed into standard quadratic programming (QP). Let $U_t = [u_{k-1}^T, \ldots, u_{k-1}^T]^T$, and define the lower triangular accumulation matrix as follows:

$$A_t = \text{tril}(\mathbf{1}),\ A_I = \text{kron}(A_t, I_{N_u}) \tag{82}$$

$$A_c = \begin{bmatrix} A_I & 0 \\ -A_I & 0 \\ SA_I & -1 \\ -SA_I & -1 \end{bmatrix} \tag{83}$$

$$b_c = \begin{bmatrix} {U_{max}}^p - U_t \\ -{U_{min}}^p + U_t \\ {U_{max}}^r - SU_t \\ -{U_{min}}^r + SU_t \end{bmatrix}, A_c z \leq b_c \tag{84}$$

$$z = \begin{bmatrix} \Delta U^{\mathrm{T}} & \varepsilon \end{bmatrix}^{\mathrm{T}},\ 0 \leq \varepsilon \leq 2^\circ \tag{85}$$

$$\min \frac{1}{2} z^T H_q z + f_q^T z,\ \text{s.t. } A_{cons} z \leq b_{cons},\ l_b \leq z \leq u_b \tag{86}$$

where A_I is the lower triangular accumulated increment matrix, S selects the front and rear steering entries, superscripts p and r denote physical and regression region bounds, respectively, and ε is the bounded non-negative slack variable. The first two block rows in Equation (83) are hard physical constraints; the final two block rows are the only softened regression region constraints.

The bound vector in Equation (84) is constructed after moving the accumulated previous input to the right-hand side. With $z = [\Delta U^T, \varepsilon]^T$, the QP uses $A_c\, z \leq b_c$. This indexing avoids the previous ambiguity between the accumulated input and the increment decision variable.

Equations (83) and (84) are the final standard inequality form. The zero slack column that appeared previously has been removed. The first two row blocks enforce physical input limits without slack; the last two steering regression row blocks contain $-1\cdot\varepsilon$, so ε directly relaxes only those bounds. The decision vector in Equation (85) therefore has a nonzero, explicitly bounded role in the QP.

The online solution uses an interior point quadratic programming solver. At each step, only the first control increment of the optimal sequence is applied, forming a receding horizon closed loop of optimization, execution, and update.

4.2. Steering Angle Constraint Based on the Regression Region

4.2.1. Regression Region Boundary and Adhesion Capability Mapping

To prevent steering commands from driving the tire into a deep nonlinear region under large sideslip, this paper constructs dynamic boundaries for the front and rear axle steering angles based on the regression-region concept. The key step is to map adhesion capability to the allowable slip angle range and then to the feasible steering angle range [19].

$$\delta_{f,c}(k) = \arctan\left(\frac{V_y + l_f r}{V_x}\right) \tag{87}$$

$$\delta_{r,c}(k) = \arctan\left(\frac{V_y - l_r r}{V_x}\right) \tag{88}$$

$$\alpha_{f,p}(k) = \arctan\left(\frac{3\overline{\mu}_k F_{z,f}}{C_f}\right) \tag{89}$$

$$\alpha_{r,p}(k) = \arctan\left(\frac{3\overline{\mu}_k F_{z,r}}{C_r}\right) \tag{90}$$

$$\delta^{reg}_{f,min}(k) = \max\left(-\delta_{f,lim},\ \delta_{f,c}(k) - \alpha_{f,p}(k)\right) \tag{91}$$

$$\delta^{reg}_{f,max}(k) = \min\left(\delta_{f,lim},\ \delta_{f,c}(k) + \alpha_{f,p}(k)\right) \tag{92}$$

$$\delta^{reg}_{r,min}(k) = \max\left(-\delta_{r,lim},\ \delta_{r,c}(k) - \alpha_{r,p}(k)\right) \tag{93}$$

$$\delta^{reg}_{r,max}(k) = \min\left(\delta_{r,lim},\ \delta_{r,c}(k) + \alpha_{r,p}(k)\right) \tag{94}$$

The above boundaries are constructed from a center value and a margin: $\delta_{f,c}, \delta_{r,c}$ gives the nominal steering center in the current state, and $\alpha_{f,p}, \alpha_{r,p}$ gives the recoverable yaw margin determined by adhesion capacity.

The minimum/maximum boundary uses max/min together with the physical upper limit of the steering angle, because the regression region constraint must satisfy both stability requirements and actuator mechanical limits.

The coefficient 3 used in the ultimate slip angle mapping is selected as a conservative engineering coefficient. The lateral tire force is approximately linear only near small slip angles and gradually enters a nonlinear saturation region as the adhesion limit is

approached. Using one third of the adhesion-dependent ultimate slip angle capacity keeps the regression boundary inside the recoverable region instead of allowing the controller to operate near the tire force saturation boundary. If the coefficient is smaller, the feasible steering interval becomes overly conservative and trajectory tracking is unnecessarily sacrificed; if it is larger, the boundary may enter the deep nonlinear tire region and reduce stability margin. Therefore, the value of 3 provides a practical compromise between path accessibility and yaw stability protection.

The state space division of the regression region constraint is shown in Figure 4.

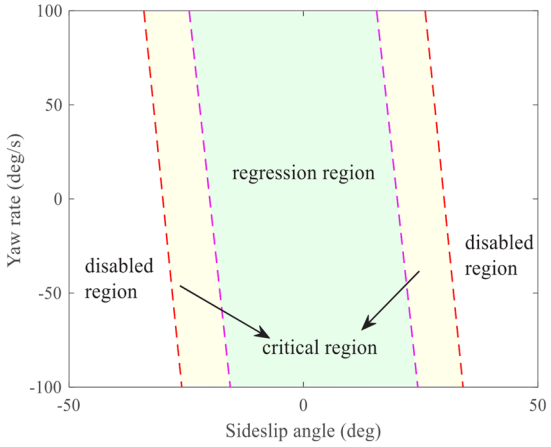


Figure 4. Schematic diagram of regression region constraints.

The green area in the figure corresponds to the recoverable regression domain, meaning that, under the current combination of center-of-mass sideslip angle and yaw angular velocity, the controller can still return the vehicle state to the stable operating region through feasible steering input. The light-colored areas on both sides are critical regions, where steering angle and torque constraints must be tightened to suppress state escape. The outer area is the failure region, where a more conservative stabilization strategy should be triggered.

The above geometric partitions correspond to $\delta_{f,min}^{reg}, \delta_{f,max}^{reg}, \delta_{r,min}^{reg}, \delta_{r,max}^{reg}$ in the boundary formula given in this section. When the state approaches the critical boundary, the feasible steering angle interval automatically shrinks; when the state returns to the central regression domain, the interval is gradually relaxed.

When adhesion decreases, $\alpha_{f,p}, \alpha_{r,p}$ decreases accordingly and the regression region shrinks synchronously. When adhesion recovers, the constraint boundary is relaxed accordingly, thereby achieving a dynamic balance between stability and accessibility.

4.2.2. Joint Constraints on Absolute and Incremental Boundaries

Based on the regression region boundary, this paper further introduces actuator amplitude and change rate constraints to form a two-layer constraint structure: state-dependent absolute boundaries and hardware-dependent incremental boundaries.

$$\delta_f(k) \in [\delta_{f,min}^{reg}(k), \delta_{f,max}^{reg}(k)] \tag{95}$$

$$\delta_r(k) \in [\delta_{r,min}^{reg}(k), \delta_{r,max}^{reg}(k)] \tag{96}$$

$$F_{x,f}(k) \in [T_{f,min}/R_w,\ T_{f,max}/R_w] \tag{97}$$

$$F_{x,r}(k) \in [T_{r,min}/R_w,\ T_{r,max}/R_w] \tag{98}$$

$$|\Delta\delta_f(k)| \le \Delta\delta_{f,max},\ |\Delta\delta_r(k)| \le \Delta\delta_{r,max} \tag{99}$$

$$|\Delta F_{x,f}(k)| \leq \Delta F_{x,f,max},\ |\Delta F_{x,r}(k)| \leq \Delta F_{x,r,max} \tag{100}$$

The first four formulas are absolute constraints that directly limit the executable control input at the current time, whereas the last two formulas are incremental constraints that restrict the control change rate between adjacent time steps. Combining these constraints ensures both stability and actuator smoothness.

In the parameter settings, the physical upper limits of the front and rear axle steering angles are $\pm 25^{\circ}$ and $\pm 10^{\circ}$, respectively; the upper limits of the steering angle increments are $\pm 2^{\circ}$ and $\pm 1^{\circ}$; and the upper limits of the front and rear axle longitudinal force increments are both $\pm 10/R_w$. This setting effectively suppresses buffeting and reduces abrupt changes in driving/braking force.

4.2.3. Closed-Loop Synergy Mechanism of IMM-AUKF and MIMO-MPC

This paper tightly couples the estimator and controller in time: IMM-AUKF first updates the adhesion estimates, and MIMO-MPC then synchronously reconstructs the model and constraints based on the updated adhesion. This closed-loop mechanism can be expressed as follows:

$$\hat{\mu}_{i,k} = \text{IMM-AUKF}(z_k),\ \overline{\mu}_k = \frac{1}{4}\sum_i \hat{\mu}_{i,k} \tag{101}$$

$$\Theta_k = \left[\tilde{C}_{\alpha}(k),\ \delta^{reg}(k),\ U_{max/min}(k)\right]^T \tag{102}$$

$$\Theta_k = \mathcal{F}(\overline{\mu}_k, x_k, u_{k-1}) \tag{103}$$

$$u_k = u_{k-1} + \Delta u_k^*,\ \Delta u_k^* = \text{argmin} J_k \tag{104}$$

This closed-loop link can be explained in three steps. First, the estimator obtains the adhesion posterior from the current observation. Second, the model parameters and constraint boundaries are updated through the mapping function $\mathcal{F}(\cdot)$. Finally, receding-horizon optimization is completed within the updated feasible region.

Therefore, the above formulas are not isolated components. They define a causal closed-loop computation chain: the estimator converts sensor and tire information into an adhesion posterior, the regression region module converts the posterior into state-dependent steering boundaries, and the MIMO-MPC optimizer computes steering and longitudinal force increments within the updated feasible set. This chain ensures that adhesion estimation, constraint update, and control allocation remain synchronized in the same time domain.

This cooperative link unifies adhesion state update, prediction model reconstruction, constraint boundary adjustment, and optimal control solution within the same receding horizon. As a result, it can continuously maintain model consistency and constraint feasibility under abrupt adhesion changes and strong maneuvers, while reducing target conflicts caused by separated lateral and longitudinal control. The following simulations quantify the performance of this closed-loop mechanism under different driving conditions.

5. Simulation Verification and Results Analysis

5.1. Double Lane Change Conditions on High Adhesion Pavement

5.1.1. Driving Condition Settings and Evaluation Indicators

The high adhesion double lane change (DLC) scenario is used to verify the trajectory tracking and attitude stabilization capabilities of the controller under highly dynamic

lane-changing conditions. The evaluation indicators include lateral error RMSE, heading error RMSE, speed error RMSE, and mean adhesion estimation RMSE.

$$RMSE_Y = \sqrt{\frac{1}{N}\sum_{k=1}^{N}\left(Y_k - Y_k^{ref}\right)^2} \tag{105}$$

$$RMSE_\phi = \sqrt{\frac{1}{N}\sum_{k=1}^{N}\left(\phi_k - \phi_k^{ref}\right)^2} \tag{106}$$

$$RMSE_{\mu,i} = \sqrt{\frac{1}{N}\sum_{k=1}^{N}\left(\hat{\mu}_{i,k} - \mu_{i,k}\right)^2} \tag{107}$$

$$RMSE_{\mu,avg} = \frac{1}{4}\sum_{i\in\{fl,fr,rl,rr\}} RMSE_{\mu,i} \tag{108}$$

The above indicators are all derived from the root-mean-square error definition. $RMSE_Y$ and $RMSE_\phi$ measure the overall magnitude of the lateral trajectory error and heading error, respectively, avoiding contingency caused by evaluating only peak values.

$RMSE_{\mu,i}$ reflects the accuracy of single-wheel adhesion estimation, and $RMSE_{\mu,avg}$ gives the overall estimator performance through four-wheel averaging, which facilitates unified comparison with the control indicators.

This scenario focuses on the lateral–longitudinal coupling stability of the vehicle during continuous large curvature lane changes and on the influence of estimation errors on control performance.

For reproducibility, the seven-degree-of-freedom Pacejka plant is integrated at 0.5 ms, while both the estimator and controller are updated every 20 ms using zero-order held commands. The proposed controller uses Np = 8, Nc = 1, ρ = 1000, and a 2 deg cap on regression bound slack. The benchmark contains a front-steering lateral MPC, an independently tuned longitudinal PID, a speed-dependent proportional rear steering rule, and a single-model UKF. Both cases use the same vehicle/tire model, reference trajectory, plant integration step, estimator/controller period, and evaluation metrics; only the estimator controller architecture differs.

The benchmark is a decoupled architecture comprising front-steering lateral MPC, independently tuned longitudinal PID, a speed-dependent proportional rear steering rule, and a single-model UKF. It uses the same vehicle/tire model, reference trajectory, 20 ms update period, and evaluation metrics. It does not include IMM probability fusion, adhesion-driven regression bound reconstruction, or joint lateral–longitudinal optimization.

5.1.2. Simulation Results and Analysis

The key performance indicators for the DLC scenario are shown in Table 1.

Table 1. Key performance indicators under high-adhesion DLC conditions.

Metric	MIMO-MPC+ IMM-AUKF	MPC+PID+ UKF
Lateral RMSE/(m)	0.2290	0.1793
Heading RMSE/(deg)	1.2427	0.4879
Speed RMSE/(m/s)	0.1833	0.7950
Mean RMSE of adhesion estimation	0.0812	0.1567

Figures 5 and 6 show bounded tracking responses in the revised high-adhesion DLC test. The proposed chain has lateral RMSE 0.2290 m and maximum lateral error 0.7007 m, compared with 0.1793 m and 0.6135 m for the benchmark. Thus, the revised DLC result does not support a lateral error advantage for the proposed tuning and is reported as such.

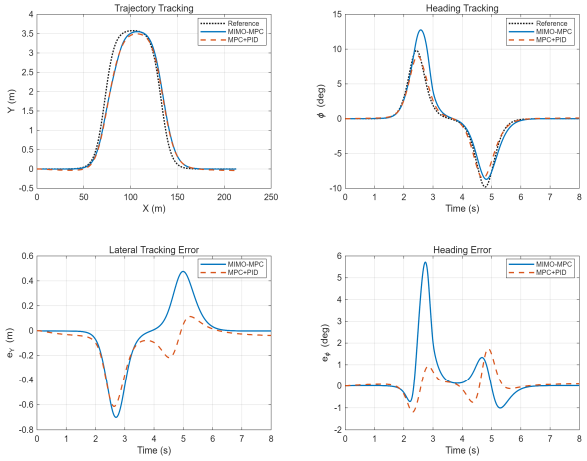


Figure 5. Trajectory tracking and error comparison under high-adhesion DLC conditions.

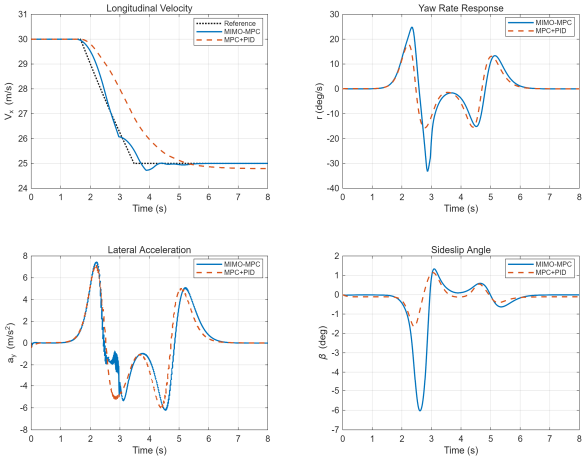


Figure 6. Comparison of key state responses under high-adhesion DLC conditions.

The DLC heading RMSE is 1.2427 deg for the proposed controller and 0.4879 deg for the benchmark; the corresponding maximum errors are 5.7141 and 1.7409 deg. The heading channel is therefore a limitation of the present coupled controller tuning rather than evidence of a uniform performance improvement.

Figure 7 shows finite rate-limited steering and longitudinal force commands. The MPC+PID benchmark has smaller and smoother command amplitudes. In the speed channel, however, the proposed controller reduces DLC speed RMSE from 0.7950 to 0.1833 m/s (76.95%) and maximum speed error from 1.8605 to 0.5788 m/s (68.89%). The QP result is accepted only when its exit status, finite values, and constraint residual are valid; otherwise, the previous physically bounded command is retained.

Figure 8 shows the revised adhesion estimation response. The mean four-wheel adhesion RMSE is 0.0812 for IMM-AUKF and 0.1567 for UKF, a reduction of 48.19%. This estimator advantage is retained even though the lateral and heading DLC metrics are not uniformly improved.

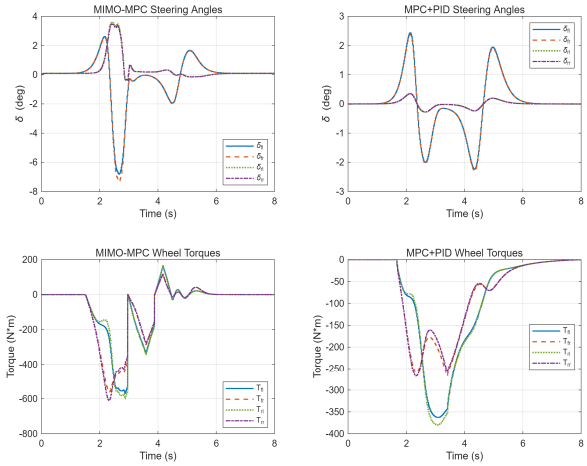


Figure 7. Control input comparison under high-adhesion DLC conditions.

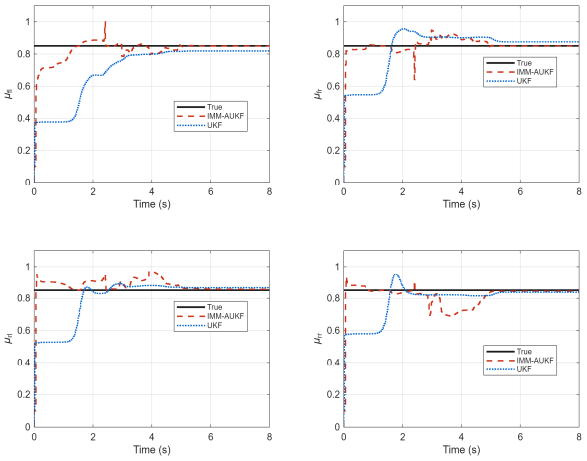


Figure 8. Comparison of adhesion estimation under high-adhesion DLC conditions.

5.2. Variable Adhesion Road Conditions

5.2.1. Driving Condition Settings and Estimator Response

The single lane change (SLC) scenario evaluates estimator convergence and closed-loop response to an adhesion step. All four-wheel adhesion coefficients are 0.85 before 3 s and 0.35 thereafter; the estimator and controller continue to update at 20 ms.

When the adhesion coefficient undergoes a step change, the multi-model weights are adaptively redistributed according to observation consistency, thereby suppressing estimation jumps and shortening the convergence process.

5.2.2. Simulation Results and Robustness Analysis

The key performance indicators for the SLC scenario are shown in Table 2.

Under the variable adhesion SLC condition, lateral RMSE decreases from 0.1816 m for the benchmark to 0.1649 m for the proposed method (9.19%), and maximum lateral error decreases from 0.6631 to 0.5942 m (10.38%). These improvements are obtained after the bounded regression region constraint is reconstructed following the adhesion step.

The SLC heading result is a trade-off that must be stated explicitly. The proposed method has heading RMSE 1.4947 deg and maximum heading error 5.2483 deg, whereas the benchmark has 0.4423 deg and 1.6471 deg. The figures show that this yaw transient is concentrated around the adhesion transition; it is not claimed to be an improvement.

Table 2. Key performance indicators under variable adhesion SLC conditions.

Metric	MIMO-MPC + IMM-AUKF	MPC + PID + UKF
Lateral RMSE/(m)	0.1649	0.1816
Heading RMSE/(deg)	1.4947	0.4423
Speed RMSE/(m/s)	0.2505	0.7983
Mean RMSE of adhesion estimation	0.0949	0.1622

Table 2 and Figures 9–12 show that the proposed method reduces SLC speed RMSE from 0.7983 to 0.2505 m/s (68.62%) and maximum speed error from 1.9063 to 0.9568 m/s (49.81%). The mean adhesion estimation RMSE decreases from 0.1622 to 0.0949 (41.51%). These gains coexist with the larger heading transient described above.

From the perspective of stability, safety, and passenger comfort, the larger SLC heading transient is a limitation of the present tuning. The proposed controller improves lateral path and speed metrics in this test, but its yaw response requires further comfort-oriented tuning, for example through explicit yaw rate, yaw acceleration, or jerk penalties.

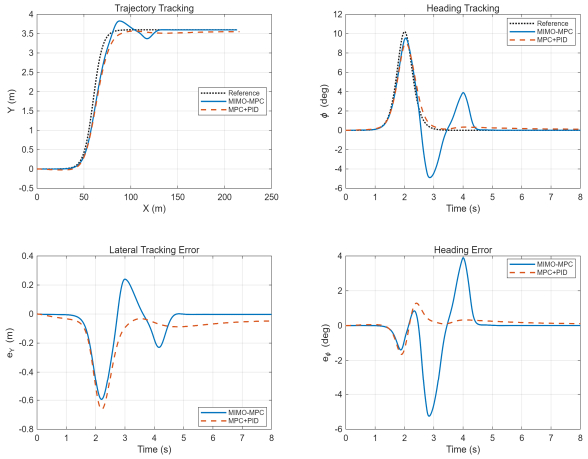


Figure 9. Trajectory tracking and error comparison under variable adhesion SLC conditions.

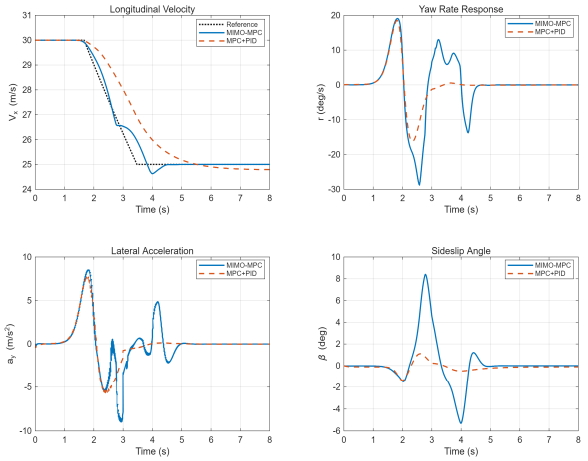


Figure 10. Comparison of key state responses under variable adhesion SLC conditions.

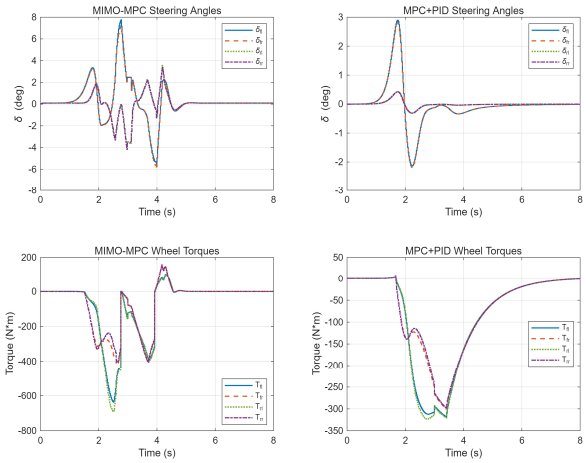


Figure 11. Control input comparison under variable adhesion SLC conditions.

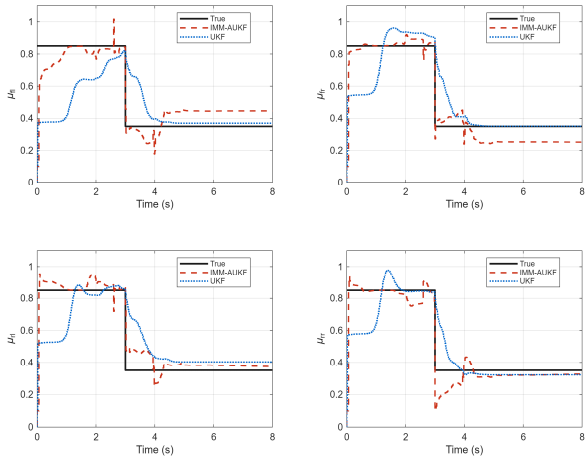


Figure 12. Comparison of adhesion estimation under variable adhesion SLC conditions.

Figure 11 shows finite command traces through the adhesion transition. The revised implementation validates the QP exit status and residual, clips every accepted command to physical limits, and limits regression bound slack to 2 deg. These safeguards prevent an infeasible numerical QP result from being propagated to the plant. The speed improvement is reported above rather than used to claim uniform performance superiority.

Figure 12 shows that the IMM-AUKF estimate reconverges after the adhesion step. Its mean adhesion estimation RMSE is 0.0949, compared with 0.1622 for the UKF. The result supports the estimator benefit under the tested adhesion transition, while not establishing general robustness for all road conditions.

5.3. Comparative Controller Performance Analysis

5.3.1. Comprehensive Analysis of the Two Driving Conditions

The revised results do not indicate a uniform advantage in every tracking channel. In DLC, the proposed chain provides substantially lower speed and adhesion estimation RMSE but larger lateral and heading errors than the benchmark. In SLC, it lowers lateral, speed, and adhesion estimation RMSE, but has a larger heading error. This metric-specific presentation replaces the earlier claim of a consistent overall trajectory maintenance advantage.

The speed channel improves in both tests: 76.95% lower RMSE in DLC and 68.62% lower RMSE in SLC. The attitude channel remains the main limitation: heading RMSE is larger for the proposed method in both revised simulations. Future tuning must explicitly

balance yaw comfort and path/speed objectives before any broader performance claim is made.

5.3.2. Mechanism and Engineering Implications

From a mechanism perspective, the framework links estimation, constraint reconstruction, and optimization. IMM-AUKF supplies the adhesion estimate, the regression module constructs a steering feasibility boundary, and MIMO-MPC allocates steering and longitudinal force under that boundary. The contribution is this causal integration and its reproducible implementation, not an assertion that every metric is improved under every condition.

Relative to the decoupled benchmark, the revised simulations show clear speed control and adhesion estimation gains and a conditional SLC lateral path gain, together with an unresolved heading response trade-off. The present results are simulation evidence only and should not be interpreted as readiness for vehicle deployment.

5.3.3. Scope of Validation and Practical Implementation Considerations

The above simulation results verify the feasibility of the proposed estimation control chain under high-adhesion DLC and variable adhesion SLC scenarios, but these two cases do not cover all road and maneuver conditions encountered by autonomous vehicles. In this paper, extreme driving conditions refer to abrupt adhesion decreases, fast lane-change steering, near-boundary regression region states, and transient tire force saturation tendencies. Split adhesion roads, extremely low-friction ice/snow surfaces, continuous curves, and emergency obstacle avoidance maneuvers may introduce stronger tire-force asymmetry, longer transient excitation, and more severe constraint conflicts. Therefore, the present results demonstrate representative simulation performance rather than complete generalization to every possible driving condition.

The readability of the simulation discussion has also been improved by standardizing figure/table captions and by explicitly connecting the quantified metrics in Tables 1 and 2 with the response trends in Figures 5–12. The heading error trade-off is now explained through the RMSE, maximum error, speed error, and adhesion estimation data rather than by adding an extra enlarged figure.

The simulations also assume that the reference trajectory, vehicle state, and key dynamic inputs are available to the controller and estimator. In real autonomous driving systems, localization drift, sensor noise, measurement delay, actuator delay, and asynchronous sampling may degrade both estimation consistency and closed-loop control accuracy. These effects should be incorporated in future hardware-in-the-loop and real vehicle tests through sensor noise injection, delay modeling, and asynchronous measurement updating.

The benchmark comparison in this paper is selected to isolate the difference between the proposed integrated framework and the commonly used decoupled architecture of lateral MPC, longitudinal PID, and single-model UKF estimation. Recent learning-based MPC, robust/adaptive MPC, sliding mode control, and advanced multi-sensor estimators also address model mismatch and uncertainty from different perspectives. Compared with these alternatives, the main emphasis of this work is the closed-loop conversion of adhesion estimation into both model parameter updating and regression region constraint reconstruction. Quantitative comparisons with these modern controllers and estimators remain necessary for a more complete state-of-the-art assessment.

Timing was measured in MATLAB R2025b on a Windows 11 desktop virtual machine. The plant ODE integration and figure/file I/O were excluded; the first five updates were discarded as warm-up. The measured controller action times are listed in Table 3. In DLC, the controller routine averaged 4.095 ms (95th percentile 7.356 ms; maximum 31.764 ms);

in SLC it averaged 4.231 ms (95th percentile 7.941 ms; maximum 42.761 ms). The corresponding estimator plus controller means were 5.061 and 5.166 ms. The virtual machine maxima do not establish hard real-time performance at 20 ms, so target embedded or hardware-in-the-loop timing remains required before deployment.

Table 3. Measured desktop timing of the online routines (MATLAB R2025b).

Metric	DLC	SLC
Controller routine mean/(ms)	4.095	4.231
Controller routine 95th percentile/(ms)	7.356	7.941
Controller routine maximum/(ms)	31.764	42.761
Estimator + controller mean/(ms)	5.061	5.166

6. Conclusions

This study establishes and verifies an IMM-AUKF-MIMO-MPC simulation chain with adhesion-driven regression region constraints. The corrected implementation uses a consistent 20 ms estimator/controller update, causal covariance correction, bounded soft regression constraints, QP feasibility validation, and physical command limiting.

IMM-AUKF improves mean adhesion estimation RMSE in both revised cases, and the coupled controller substantially improves speed tracking. The revised SLC case also improves lateral RMSE. However, the heading metrics are worse than the benchmark in both cases; this limitation is retained in the conclusions rather than masked by aggregate claims.

The desktop timing results show that mean online computation is below the 20 ms update interval, but virtual machine maxima exceed that interval. Consequently, the work provides reproducible simulation evidence and a defined implementation baseline, not a claim of embedded real-time readiness.

Future work will include embedded or hardware-in-the-loop timing, real vehicle tests, split adhesion and low-friction surfaces, sensor noise and delay, and comfort-oriented yaw/jerk tuning. These extensions are required to assess generalization, hard real-time feasibility, and passenger comfort performance.

Author Contributions: Conceptualization, Q.L. and C.J.; methodology, Q.L. and J.P.L.; software, Q.L.; validation, Q.L., C.J. and J.W.; formal analysis, Q.L. and C.J.; investigation, Q.L. and C.J.; resources, J.W.; data curation, Q.L.; writing—original draft preparation, Q.L.; writing—review and editing, J.W. and J.P.L.; visualization, Q.L.; All authors have read and agreed to the published version of the manuscript.

Funding: This research was funded by the University-Industry-Collaborative Innovation Fund of Chinese Universities, grant number 2022BC071; and the Science and Technology Research Project of Jiangxi Provincial Department of Education, grant numbers GJJ2405101 and GJJ2505013.

Data Availability Statement: The raw data supporting the conclusions of this article will be made available by the authors on request.

Acknowledgments: The authors would like to thank the editor and reviewers for providing valuable review comments.

Conflicts of Interest: The authors declare no conflicts of interest.

References

1. Cao, H.; Zhao, S.; Song, X.; Bao, S.; Li, M.; Huang, Z.; Hu, C. An optimal hierarchical framework of the trajectory following by convex optimisation for highly automated driving vehicles. *Veh. Syst. Dyn.* **2019**, *57*, 1287–1317. [CrossRef]
2. Cui, Q.; Ding, R.; Wei, C.; Zhou, B. Path-tracking and lateral stabilisation for autonomous vehicles by using the steering angle envelope. *Veh. Syst. Dyn.* **2021**, *59*, 1672–1696. [CrossRef]

3. Zhang, Z.; Xie, L.; Lu, S.; Wu, X.; Su, H. Vehicle yaw stability control with a two-layered learning MPC. *Veh. Syst. Dyn.* **2023**, *61*, 423–444. [CrossRef]
4. Zhang, Y.; Wang, W.; Wang, W.; Yang, C.; Zhang, Y. An adaptive constrained path following control scheme for autonomous electric vehicles. *IEEE Trans. Veh. Technol.* **2022**, *71*, 3569–3578. [CrossRef]
5. Shao, L.; Jin, C.; Lex, C.; Eichberger, A. Robust road friction estimation during vehicle steering. *Veh. Syst. Dyn.* **2019**, *57*, 493–519. [CrossRef]
6. Xu, Y.; Chen, B.; Chi, C. Estimation of road friction coefficient and vehicle states by 3-DOF dynamic model and HSRI model based on information fusion. *Asian J. Control* **2018**, *20*, 1067–1076. [CrossRef]
7. Wielitzka, M.; Ortmaier, T. Credibility of state and friction coefficient estimation in vehicle dynamics using UKF. In *Proceedings of the 2019 IEEE 58th Conference on Decision and Control, Nice, France, 11–13 December 2019*; IEEE: New York, NY, USA, 2019; pp. 3922–3927.
8. Heidfeld, H.; Schuneimann, M.; Kasper, R. UKF-based state and tire slip estimation for a 4WD electric vehicle. *Veh. Syst. Dyn.* **2020**, *58*, 1479–1496. [CrossRef]
9. Fu, X.; Sun, W.; Huang, B.; Xing, A.; Wang, J. Estimation of road adhesion coefficient based on fading memory unscented Kalman filtering with exponential weighting. *Automot. Technol.* **2018**, *1*, 31–37.
10. Liu, Z.; Liu, Y. Estimation algorithm for road adhesion coefficient using adaptive fading unscented Kalman filter. *China J. Highw. Transp.* **2020**, *33*, 176–185.
11. Luo, Z.; Fu, Z.; Xu, Q. An adaptive multi-dimensional vehicle driving state observer based on modified Sage-Husa UKF algorithm. *Sensors* **2020**, *20*, 6889. [CrossRef] [PubMed]
12. Zhang, J.; Li, J. Vehicle state estimation based on interactive multiple model and cubature Kalman filter. *Automot. Eng.* **2017**, *39*, 977–983.
13. Liang, J.; Lu, Y.; Yin, G.; Fang, Z.; Zhuang, W.; Ren, Y.; Xu, L.; Li, Y. A distributed integrated control architecture of AFS and DYC based on MAS for distributed drive electric vehicles. *IEEE Trans. Veh. Technol.* **2021**, *70*, 5565–5577. [CrossRef]
14. Zhao, J.; Wong, P.K.; Ma, X.; Xie, Z. Chassis integrated control for active suspension, active front steering and direct yaw moment systems using hierarchical strategy. *Veh. Syst. Dyn.* **2017**, *55*, 72–103. [CrossRef]
15. Wang, G.; Liu, Y.; Li, S.; Tian, Y.; Zhang, N.; Cui, G. New integrated vehicle stability control of active front steering and electronic stability control considering tire force reserve capability. *IEEE Trans. Veh. Technol.* **2021**, *70*, 2181–2195. [CrossRef]
16. Zheng, K.; Zhou, B.; Wu, X.; Chai, T.; Pan, Q. A humanoid collision-avoidance strategy considering a large sideslip angle state. *Control Eng. Pract.* **2023**, *138*, 105623. [CrossRef]
17. Deng, H.N.; Zhao, Z.G.; Zhao, K.; Li, G.; Yu, Q. Estimation of road adhesion coefficient using interactive multiple model adaptive unscented Kalman filter for 4WID vehicles. *Automot. Eng.* **2024**, *46*, 1357–1369. [CrossRef]
18. Liu, J.; Jayakumar, P.; Stein, J.L.; Ersal, T. A nonlinear model predictive control formulation for obstacle avoidance in high-speed autonomous ground vehicles in unstructured environments. *Veh. Syst. Dyn.* **2018**, *56*, 853–882. [CrossRef]
19. Du, X.; Htet, K.K.K.; Tan, K.K. Development of agenetic-algorithm-based nonlinear model predictive control scheme on velocity andsteering of autonomous vehicles. *IEEE Trans. Ind. Electron.* **2016**, *63*, 6970–6977. [CrossRef]
20. Kim, E.; Kim, J.; Sunwoo, M. Model predictive control strategy forsmooth path tracking of autonomous vehicles with steering actuator dynamics. *Int. J. Automot. Technol.* **2014**, *15*, 1155–1164. [CrossRef]

Disclaimer/Publisher's Note: The statements, opinions and data contained in all publications are solely those of the individual author(s) and contributor(s) and not of MDPI and/or the editor(s). MDPI and/or the editor(s) disclaim responsibility for any injury to people or property resulting from any ideas, methods, instructions or products referred to in the content.